6

Mn-Substituted (Fe$_3$C/Fe$_3$O$_4$)/C nanocomposites

6.1 Introduction

The nanocomposites of Fe$_3$O$_4$ or Fe$_3$C or Fe$_3$O$_4$/Fe$_3$C with carbon are exploited as anode material for Li-ion batteries due to their higher theoretical capacities. Therefore, the present chapter describes the charging capacity of nanocomposites of carbon with Fe$_3$C or Mn$_r$Fe$_{3-r}$C/Mn$_s$Fe$_{3-s}$O$_4$ (where $0.2 \leq r+s \geq 0.7$) in addition to their structural, magnetic and biological characteristics. The continuous improvement in the discharge capacity for Fe$_3$O$_4$, Fe$_3$C or their composites with or without C was the reason for evaluating the electrochemical behaviour of these nanocomposites. Hence, we synthesized Fe$_3$C/C and Mn-substituted (Fe$_3$C and Fe$_3$O$_4$)/C nanocomposites by a simple and inexpensive sol-gel method. The purpose of Mn substitution in the Fe$_3$C/Fe$_3$O$_4$ was to observe the effect on various properties. The electrochemical performance of these nanocomposites were studied extensively using Voltammograms profiles, Galvanostatic lithiation/delithiation profiles, and Coulombic efficiencies. Further, the magnetic hyperthermia efficacy of these nanocomposites based ferrofluids (10 mg/mL) were examined in a field of 23 mT. The biocompatibility of bare particles of one of the nanocomposites i.e. M2FOC was also evaluated with human lung adenocarcinoma A549 cells after 48 h of treatment. Similar to earlier samples, the presence of Fe$_3$C, Fe$_3$O$_4$, and

carbon phases was validated by x-ray and electron diffractions. The bright-field micrographs obtained from the transmission electron microscope (TEM) recommend their nanometric dimensions. The oxidation states of the elements present in the nanocomposite M7FOC were analyzed by X-ray photoelectron spectroscopy. Further, the hyperfine parameters and identification of the phases, as well as their relative quantification, were endorsed by Mössbauer spectroscopy.

6.2 Results and discussion

6.2.1 Structural and phase analysis

The XRD patterns for all the nanocomposites *viz.* FC, M2FOC, and M7FOC are presented in Figure. 6.1. The diffraction peaks for the FC nanocomposite matched with orthorhombic Fe_3C (JCPDS no. 64-2413) and the peak for the graphitic carbon (JCPDS no. 89-8487). In contrast, for the remaining samples (*e.g.* M2FOC, and M7FOC), the patterns were resembling the Fe_3C, Fe_3O_4 (JCPDS no. 65-3107) and carbon phases. For all the samples, the graphitic carbon was noticed at 26.55º (002). The X'pert high score plus software was employed to find out the percentage proportion of the phases in the nanocomposite and the obtained values are mentioned in Fig. 6.1. Nevertheless, the nanocomposite FOC ($Fe_3C/Fe_3O_4/C$) was also prepared which contained 82% of Fe_3C and 18% of Fe_3O_4 phase (Fig. 5.1 a). Moreover, the exact distribution of Mn in the Fe_3C and Fe_3O_4 phases was quite challenging to find out. But, it is noticeable that on increasing the Mn substitution, the content of the oxide phase also enhanced. Thus, it can be argued that Mn has promoted the formation of oxide phase. Scherrer's equation estimated the crystallite size for the samples and the values lie between 7 and 13 nm (Table 6.1). A

minor variation in the crystallite size with increased Mn substitutions was noticed. The alteration in the lattice parameter for both the phases (*viz.* Fe_3C and Fe_3O_4) with enhanced Mn content is presented in Table 6.1. It has been perceived that with improved Mn substitution, the lattice parameter for both carbide and oxide phases enhanced minutely (Table 6.1).
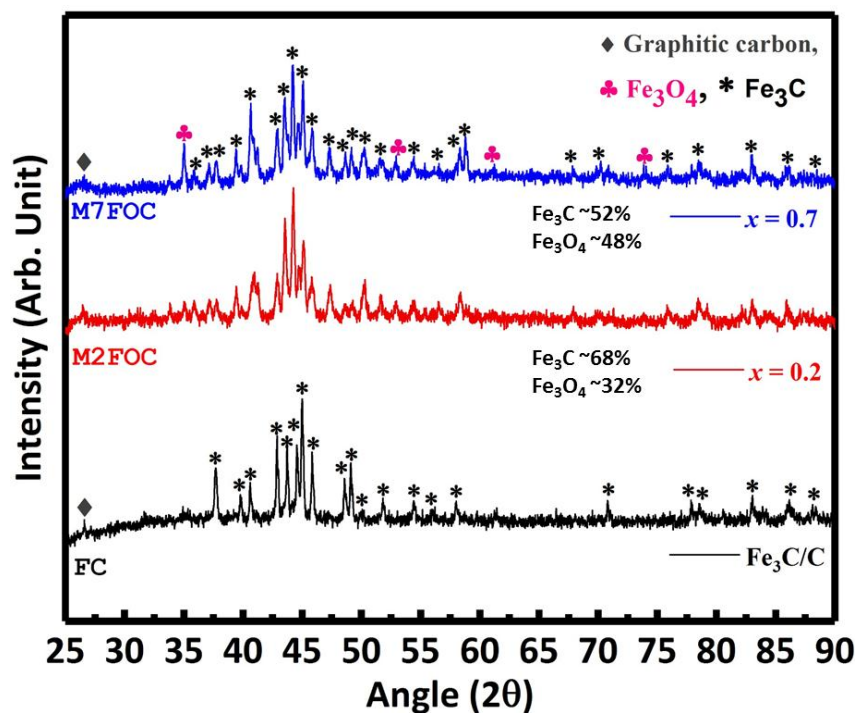

Figure 6.1: X-ray diffraction patterns for the FC, M2FOC, and M7FOC samples.

Table 6.1: Details of the structural parameters obtained from Rietveld refinement by automatic Fullprof Match! Software.

Sr. no.	Sample	Lattice parameter (a, b, c) (Å)		Angles (º)	Crystallite size (nm)	
		Fe_3C	Fe_3O_4	α, β, γ	Fe_3C	Fe_3O_4
1	FC	5.0929, 6.7467, 4.5285	---	90	~ 7	~ 9
2	M2FOC	5.0930, 6.7470, 4.5286	8.362	90	~ 9	~ 10
3	M7FOC	5.0931, 6.7473, 4.5288	8.369	90	~ 10	~ 9

It was also revealed in the XRD patterns that the peak positions get shifted slightly towards left. It could be ascribed to the variation in the atomic radii of Fe and Mn as well as ionic radii of Fe^{2+}, Fe^{3+}, and Mn^{2+} ions. The ionic radii of Fe^{2+} and Fe^{3+} ions are reported as 0.92 and 0.79 Å respectively at octahedral voids whereas 0.77 and 0.63 Å at tetrahedral sites, respectively. However, the proclaimed ionic radii for Mn^{2+} ions are 0.80 and 0.97 Å at tetrahedral and octahedral sites, respectively. Relatively bigger ionic radii of Mn^{2+} ions caused a continuous upsurge in the lattice parameter for the oxide phase. Similarly, the respective atomic radii for Fe and Mn are 1.26 and 1.27 Å. The comparatively larger radius of Mn caused consistent advancement in the lattice parameter of the Fe_3C phase.

6.2.2 Transmission electron microscopy

The morphological and microstructural properties for the sample M2FOC was investigated with the help of TEM and shown in Fig. 6.2. The bright-field micrograph of the sample suggests the presence of spherical shaped particles (Fig. 6.2 a). Moreover, the contrast difference in the bright field image may be attributed either to the distinct phase or to the overlapped particles. The SAED pattern of the M2FOC is shown in Fig. 6.2 (b), which was analyzed using ImageJ software. The obtained d spacing values for one type of diffraction pattern were 3.37, 2.54, 1.77, 1.67, 1.53 and 1.33 Å, which

resembled the (020), (200), (122), (040), (440) and (123) planes respectively for Fe_3C phase. Moreover, the d spacing 1.483 Å for the plane (440) corresponded to the Fe_3O_4 phase. The high resolution micrograph indicated two intersecting fringes resembling the presence of two phases in the system (Fig. 6.2 c).
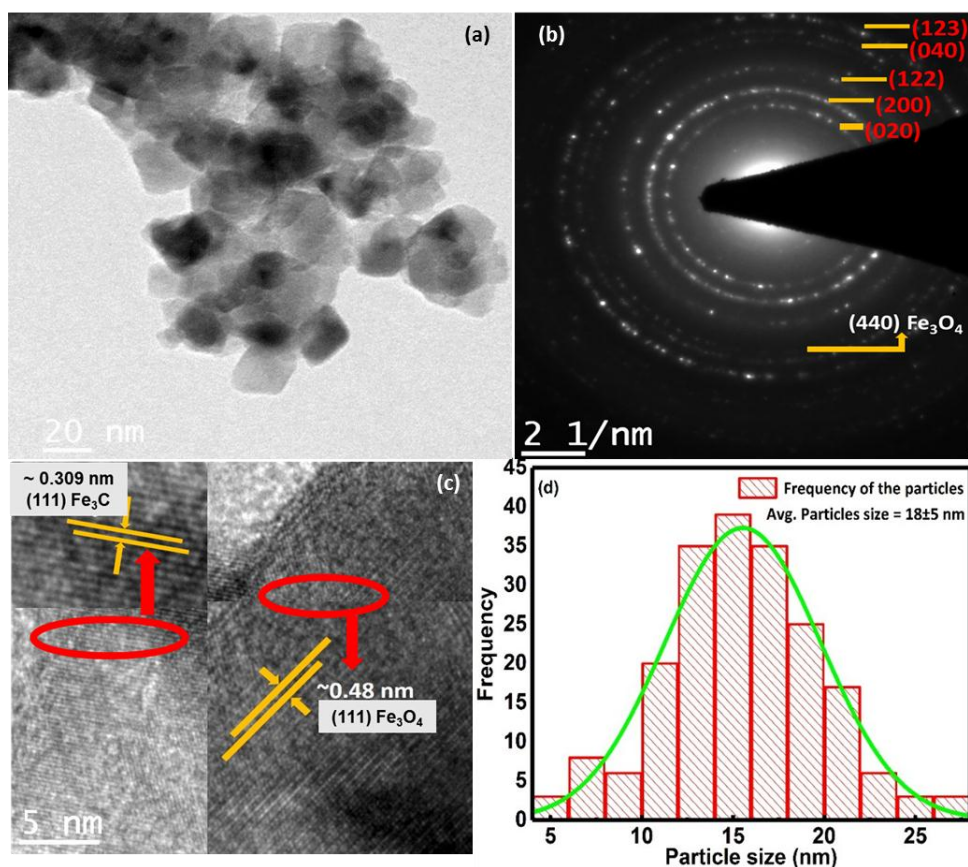

Figure 6.2: Morphological analysis for the nanocomposite M2FOC a) bright field image b) high resolution micrograph c) SAED pattern and d) histogram for the particle size.

The interplanar fringe spacing assessed using ImageJ software gave two values i.e. 0.309 and 0.48 nm. The former can be identified as (111) plane for the Fe_3C phase and the latter as (111) for Fe_3O_4. Hence, the electron diffraction and HRTEM micrograph justify the X-ray diffraction findings. The size of the particles of the nanocomposite was

found to be in the range of 5-27 nm, and the average size was ~18±5 nm (Fig. 6.2 d). This estimation was carried out using 200 particles and employing a standard normal distribution function.

Similarly, M7FOC composite was also analyzed using TEM/HRTEM to visualize the effect of Mn substitution over the morphology of the nanoparticles (Fig. 6.3 a). The SAED pattern for the sample had ring patterns favoring the polycrystalline nature. The patterns indexed with ImageJ software displayed d spacing values of 2.38, 1.85, 1.35, and 1.4 Å, which corresponded to the planes (121), (221), (302), and (240) respectively of Fe_3C phase (Fig. 6.3 b). Further, the other two planes (400) and (511) and accorded d-spacing values measured ~2.09, and 1.61 Å respectively endorsed the existence of the Fe_3O_4 phase (Fig. 6.3 b). The interplanar fringe spacing of 0.37 nm represented the (011) plane of the Fe_3C phase, whereas 0.29 nm spacing indicated (220) the plane of Fe_3O_4 phase (Fig. 6.3 c).
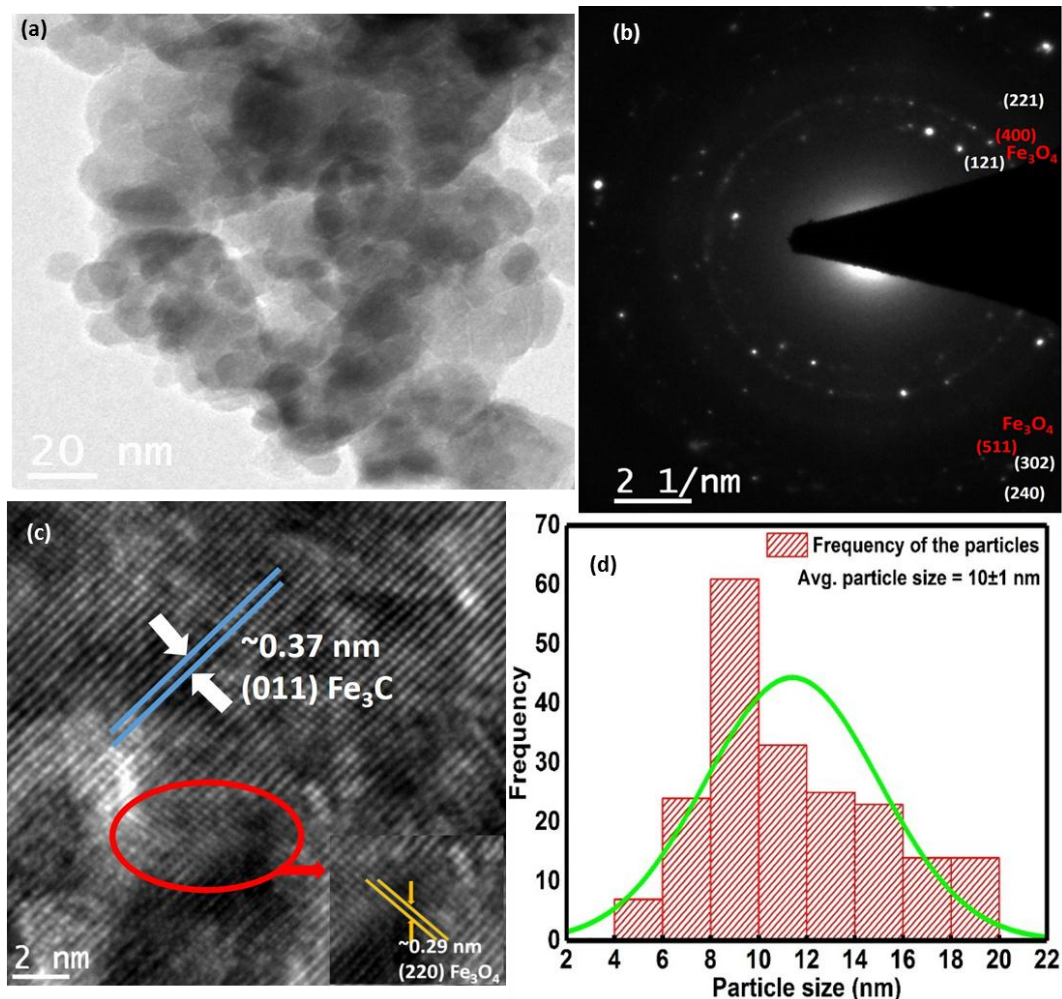
Figure 6.3: TEM analysis for the nanocomposite M7FOC a) bright field image b) high resolution micrograph c) SAED pattern and d) histogram for the particle size.

For this sample, the SAED pattern and HRTEM image validated the coexistence of two phases. The size range of the particles for the nanocomposite was 4-20 nm, and the average size of the particles was ~10±1nm (Fig. 6.3 d). Therefore, It can be extrapolated that the particle size reduces slightly with an increase in Mn substitution. The structural and morphological studies using HRTEM for Fe_3C/C sample are presented in chapter 3 and hence not discussed here.

6.2.3 XPS analysis

X-ray photoelectron spectroscopy (XPS) is a highly surface sensitive technique used for identifying the chemical states of the elements present in the sample. The XPS spectrum of the Mn-substituted nanocomposite M7FOC is exhibited in Fig. 6.4. The XPS spectrum revealed the existence of the Fe, C, Mn, and O over the surface of the sample. The spectrum of Fe 2p was deconvoluted into four peaks at 711.42, 724.9, 719.37, and 732.92 eV (Fig. 6.4 a). The peaks at 711.42 and 724.9 eV can be ascribed to Fe $2p_{3/2}$ and Fe $2p_{1/2}$ respectively for Fe, which is a component of the Fe_3C phase (Fig. 6.4 a). The other two peaks at 719.37 eV and 732.92 eV are designated as the satellite feature for Fe $2p_{3/2}$ and Fe $2p_{1/2}$ respectively corresponding to $Fe^{3+,}$ and Fe^{2+} states present in Fe_3O_4 phase (Fig. 6.4 a). The spectrum for the C 1s is shown in Fig. 6.4 (b). The decoupled peaks of this spectrum at 284.9 and 286 eV may be attributed to the C-C and C-O-C due to sp^2 and sp^3 hybridization, respectively. Moreover, Fig. 6.4 (c) represents the Mn 2p spectrum, where two peaks were obtained at 641.91 and 653.56 eV after the deconvolution. These two peaks represent the Mn 2p3/2 and Mn 2p1/2 states for the metallic Mn which was substituted in the Fe_3C phase. In contrast, the satellite peak observed at 647.24 eV, might be designated for the bonding between Mn-O. This may be attributed to the formation of the $Mn_sFe_{3-s}O_4$ phase.
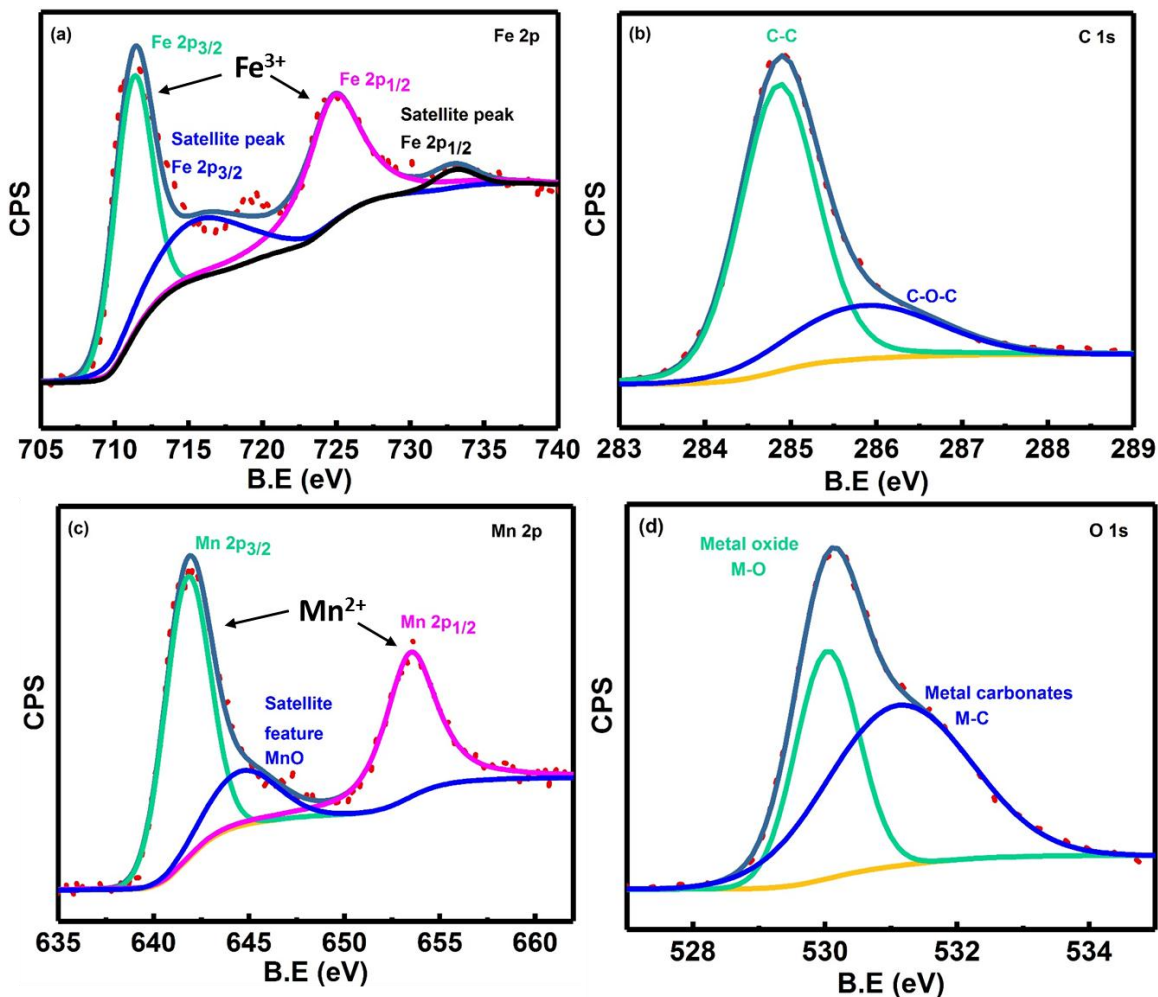
Figure 6.4: XPS spectra for the sample M7FOC after the decovolution of the peaks a) Fe 2p b) C 1s c) Mn 2p and d) O 1s.

These findings were following the XRD observations which suggested that Mn got substituted in both the carbide and oxide phases. Moreover, the spectrum for the O 1s is shown in Fig. 6.4 (d). The spectrum was deconvoluted into two peaks at 530.13 and 531.24 eV, which were ascribed to the metal-oxygen (M-O) and metal carbonates (M-C-O) bondings, respectively.

6.2.4 Mössbauer spectroscopy

Mössbauer spectroscopy was utilized to ascertain the number of phases and their respective compositions based on their magnetic behavior. Mössbauer spectra were collected for two nanocomposites M2FOC and M7FOC at ambient conditions (Fig. 6.5). The magnitudes for the magnetic hyperfine fields (B_{hf}), quadruple splitting (QS, Δ), isomer shift (IS, δ), line width (Γ), and relative area (R_A) are summarized in Table 6.2 whereas the values for FC are given in chapter 3. The spectrum for M2FOC nanocomposite was fitted with four sextets and a doublet. The first two sextets A and B represent Fe_3C phase having B_{hf} values of 21.49 and 18.46 T respectively. On the other hand, the B_{hf} values 49.1 and 41.32 T corresponded to the sextets C and D for the Fe_3O_4 phase. Out of the two, the former represents tetrahedral site and the latter one indicates octahedral site. Likewise Fe_3C sample (Fig. 3.5) a doublet was also observed for this sample, which represents the superparamagnetic component and the R_A value for this doublet was ~ 10 % (Table 6.2).
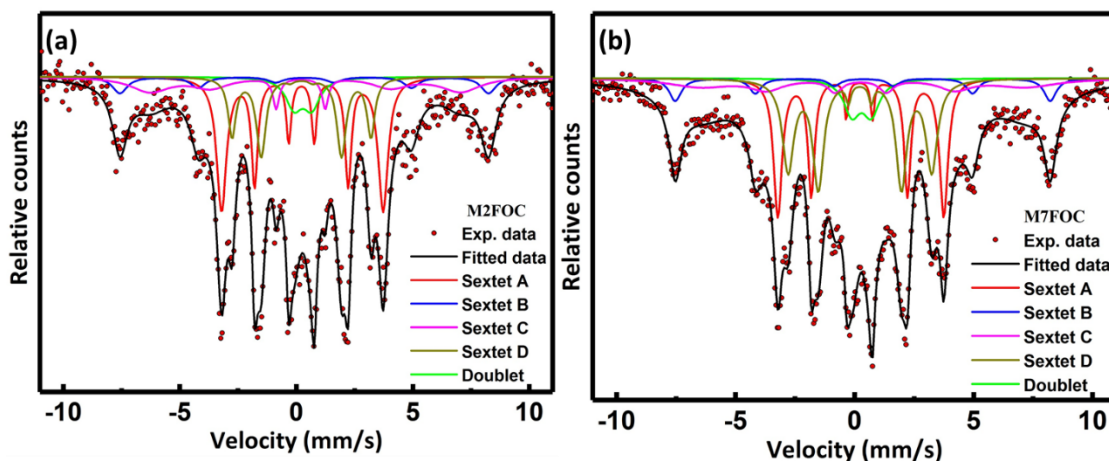

Figure 6.5: Mossbauer spectrum for the nanocomposites M2FOC and M7FOC samples.

Similarly, the spectrum for M7FOC nanocomposite was also fitted with four sextets and a doublet. The B_{hf} values for the sextets A and B were found to be as 21.61 and 18.69 T for two sites of Fe in Fe_3C. In contrast, the other two sextets C and D had B_{hf} values of 48.84 and 42.36 T indicated for tetrahedral and octahedral sites for Fe_3O_4.

Table 6.2: The hyperfine field magnitude (B_{hf}), isomer shift (δ), quadrupole splitting (Δ), inner line width (Γ) and relative area (R_A) of Fe-sites for two nanocomposites. Isomer shift values are relative to Fe metal foil ($\delta = 0.0$ mm/s).

Sample	Iron site	Hyperfine field (B_{hf}) T ± 0.01	Quadruple splitting, (Δ)mm/s ± 0.02	Isomer shift (δ) mm/s ± 0.01	Outer line width, (Γ) mm/s	Relative Area (R_A) ± 0.03 %	χ^2
	Sextet A	21.49	0.0397	0.2393	0.506	37	
M2FOC	*Sextet B*	18.46	0.0083	0.218	0.404	27	
	Sextet C	41.32	0.2062	0.289	2.08	14	1.3
	Sextet D	49.1	-0.0226	0.351	0.77	12	
	Doublet	-	0.7613	0.168	0.85	10	
	Sextet A	21.61	0.0614	0.232	0.43	19	
	Sextet B	18.69	0.0051	0.2234	0.577	23	
M7FOC	Sextet C	42.36	0.1096	0.3128	3.2	33	1.2
	Sextet D	48.84	-0.05	0.3694	0.612	14	
	Doublet	-	0.81	0.2939	0.833	11	

The B_{hf} values were lesser than that of bulk values, which could be attributed to the presence of Mn^{2+} ions and the smaller sized particles. The IS values were minutely altered due to Mn-substitution in the nanocomposites. The isomer shift and quadruple shifting values were also found to be closer to the M2FOC nanocomposite. Also, the R_A for the two sextets A and B represents the Fe_3C, which is around 42%, whereas the sextets C and D had approximately 47% for Fe_3O_4. The R_A for the doublet was 11%,

which indicated a minor increase of superparamagnetic component. It is to be noticed that the composite consisted of both Fe_3O_4 and Fe_3C phases and their estimated percentage compositions were similar to the values shown in Fig. 6.1.

6.2.5 Magnetic properties measurement

The magnetic properties of the nanocomposite samples in the field range ± 2T are shown in Fig. 6.6. The M_S values for the composites M2FOC and M7FOC are found to be around 55.58 and 34 Am^2/kg respectively. As stated earlier, on increasing Mn content, the carbide phase gradually reduced (Fig. 6.1). Therefore, sample M7FOC showed lesser M_S value than that of M2FOC. The lower M_S values for higher Mn substituted Fe_3C has been observed earlier also [118]. It has been argued that antiferromagnetic coupling of Mn with Fe reduces the M_S value. Further, inset of this figure shows the variation in the M_r and H_C values. For the composites M2FOC and M7FOC, the M_r values were estimated as 2.53 and 1.29 Am^2/kg, whereas the H_C values were noticed as 11.75 and 11.6 mT respectively. The observation further suggests that on increasing Mn substitution, the M_r value slightly decreased but the H_C values were almost unaltered.
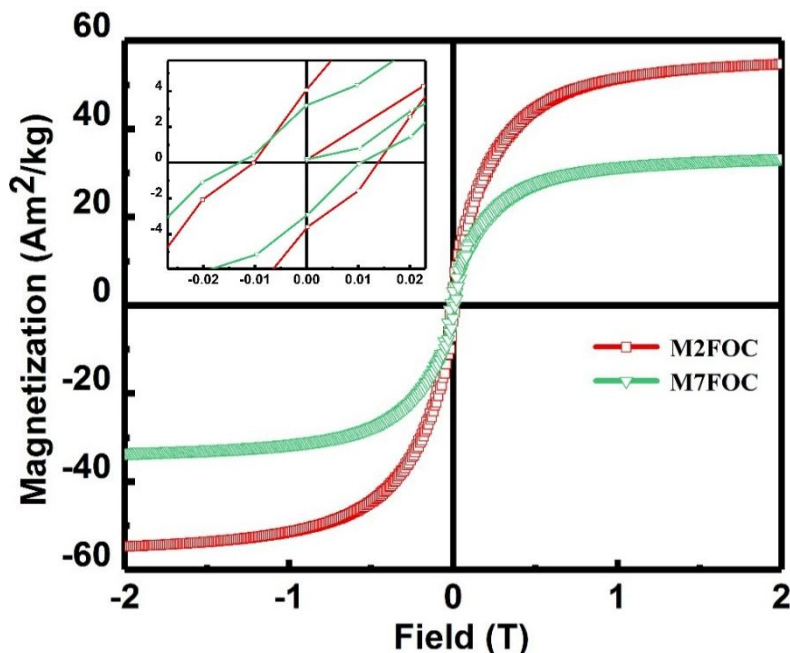
Figure 6.6: Magnetic properties of the nanocomposites M2FOC and M7FOC samples.

6.2.6 Heating efficacy

The magnetothermic behavior of ferrofluids of the nanocomposites (e.g. M2FOC and M7FOC) are shown in Fig. 6.7. The concentration of the ferrofluids were taken as 10 mg/mL and exposed to an external AC magnetic field of amplitude 23 mT and frequency 261 kHz. The heating rate for the sample M2FOC was considerably higher than that of M7FOC (Fig. 6.7). It might be due to superior M_S value for the former (Fig. 6.6). It was noticed that temperature rose continuously for both the samples with higher initial heating rate. Further, the time required to attain therapeutic temperature (~ 42 ℃) was 454 and 994 s for M2FOC and M7FOC samples respectively. The SLP values were estimated to be as 31 and 16 W/g for the M2FOC and M7FOC sample respectively.
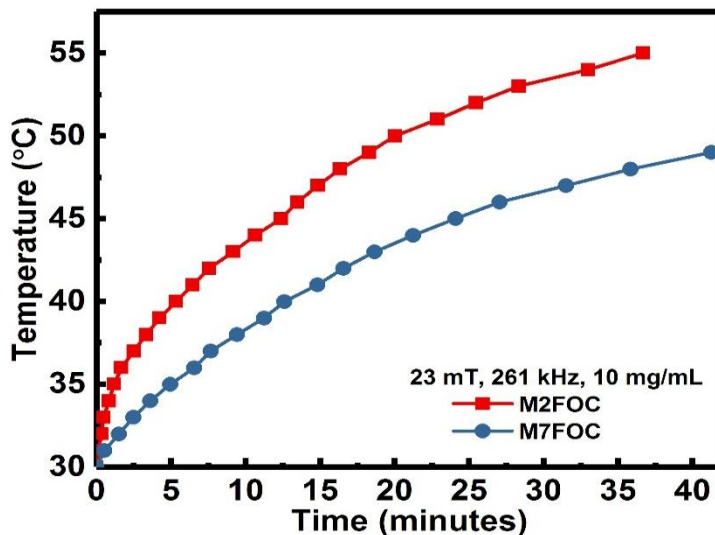
Figure 6.7: Temperature *vs.* time plots for the ferrofluids of M2FOC and M7FOC samples.

The ILP value was 0.35 and 0.18 nHm^2/kg for M2FOC and M7FOC composites respectively. The SLP and ILP values of these ferrofluids were comparable to some of the reported values but inferior to few of them [10, 25, 71, 147]. Therefore, it can be concluded that these MNP$_S$ can also be utilized for the MHT application.

6.2.7 Cytotoxicity study

The biocompatibility of bare particles of M2FOC nanocomposite was evaluated after treatments with A549 cells for 48 h. The % cell viability at different concentrations such as 0.1, 0.5, 1, 1.5, 2, 2.5 and 3 mg/mL was observed to be as 86, 80, 76, 73, 68, 66 and 64 respectively (Fig. 6.8 a). It can be persumed that a concentration of 0.1 mg/mL may be compatible with A549 cells. The % cell viability contineously diminished with increased concentration of MNPs similar to other samples as well as reported in the literature. Besides of higher concentration of Mn, the presence of the mixed phases in

the nanocomposite might be the reason for the inferior biocompatibility than pure Fe_3C or Fe_3O_4 MNPS. However, it needs extensive studies to confirm the biocompatibility. Moreover, the fluorescence micrograph of the A549 cells treated with 0.1 mg/mL of MNPs for 24 h suggest normal growth of the cells (Fig. 5.8 b). There was no alteration in the morphologies of the cells even after physical and chemical interactions with the MNPs.
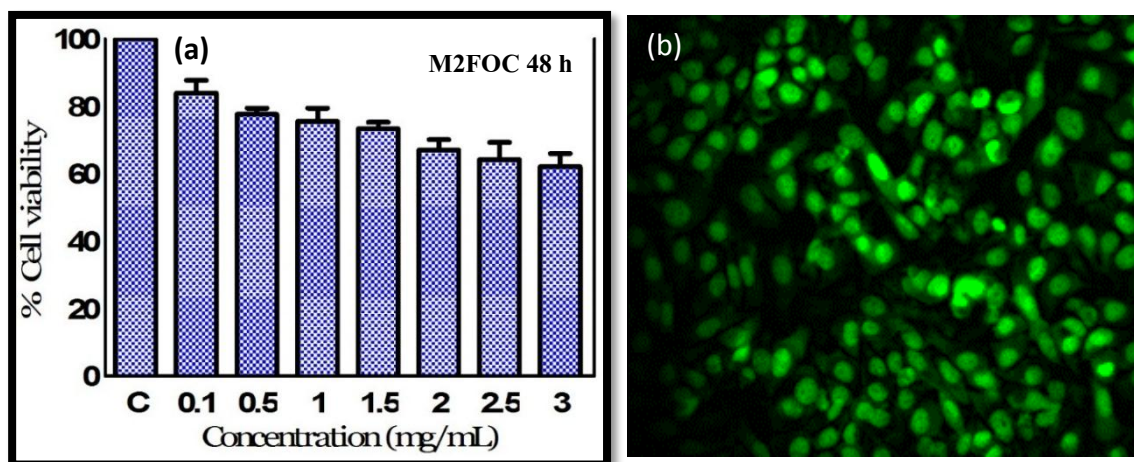

Fig. 6.8: *In-vitro* study of M2FOC nanocomposite with A549 lung cancer cell lines. a) % cell viability with varying concentrations 0.1, 0.5, 1, 1.5, 2, 2.5 and 3 mg/mL b) Fluorescence microscopy after stained with acridine orange.

6.2.8 Evaluation of the electrochemical performance

The electrochemical performance of the nanocomposites FC, M2FOC, and M7FOC are shown in Figs. 6.9, 6.10, and 6.11 respectively. For the first three cyclic Voltammograms (CV) curves for the electrode, FC (Fig. 6.9 a) were collected between 0.01 to 3.0 V at a scan rate of 0.1 mV/s in ambient condition. For the 1st discharge cycle, the prominent cathodic peaks were observed at ~0.7 and 1.67 V (*vs.* Li/Li^{+}) due to the reduction reactions on the electrode surfaces as well as at the interfaces, which causes

the formation of the SEI with LiO_2 (Fig. 6.9 a). A shift in the cathodic potential peak (~ 0.7 V) was observed during 2nd and 3rd cycles to 0.79, 0.776 V, respectively. Such increment may be ascribed to the diminished polarization after the 1st cycle. On the other hand, two peaks were also noticed at ~1.57 and ~2.35 V for the 1st cycle while charging due to the depletion of the SEI layer (Fig. 6.9 a). Nevertheless, after the 1st cycle, the intensities of the current peaks for charging/discharging and the area of CV curves were significantly reduced (Fig. 6.9 a). It indicated an irreversible oxidation of SEI film after the alteration in the structural reorganization during 1st cycle. Furthermore, Fig. 6.9 (b) represents the lithiation/delithiation profiles for sample FC between 0.01-3 V and at the rate of C/20. The sample delivered a lithium storage capacity of 827.18 mAhg^{-1} during the first discharge process. It was higher than the values reported for Fe_3C/C composite, but lower than that for the core-shell structures (viz. $Fe_3C@C$). Further, the storage capacity continuously decreased to ~144 mAhg^{-1} after the 5th cycle (Fig. 6.9 b). The sample has shown an irreversible capacity even after the fifth cycles which suggest a regular change in the structural integrity (Fig. 6.9 b). The specific discharge capacity for the respective cycles, 1st to 5th, was observed as 827.18, 596.7, 540.4, and 177.6 mAh g^{-1} (Fig. 6.9 b). Further, the magnitude of the capacity during charging was estimated to be 600, 540.8, 285.3, and 143.44 mAh g^{-1} respectively after 1st to 5th cycles (Fig. 6.9 b). Besides, each discharge profile has a potential plateau between 0.71-1.74 V, which might be due to irreversible reaction occurred after each cycle (Fig. 6.9 b). The CV curves also supported this electrochemical behavior which was noticed as a continuous reduction in the loop area (Fig. 6.9 a). However, a sharp plateau observed for the second charging cycle could be accomplished to a depletion of the SEI film over the electrode with

electrolyte. The figure 6.9 (c) shows the charge-discharge capacities and columbic efficiencies for the nanocomposite FC *vs.* cycle numbers. The initial coulombic efficiency (CE) was found to be around 72.5% for the sample (Fig. 6.9 c). The relatively low initial CE might be due to irreversible capacity loss, including the inevitable formation of SEI and decomposition of electrolyte, which are commonly observed for the anode materials. The specific charge capacity decreased from 600 to 78 mAh g^{-1} after 10 cycles and then reduced to 60 mAh g^{-1} after 25 cycles (Fig. 6.9 c). However, the initial coulombic efficiency for the initial cycle was about ~ 94%, which is comparable to the reported value for the $Fe_3C@C$ (Fig. 6.9 c). Further, as the FOC sample did not have Mn thus the oxide component was too low to display significant rise in the capacity w.r.t. FC sample. Hence, we did not perform this study for FOC sample.
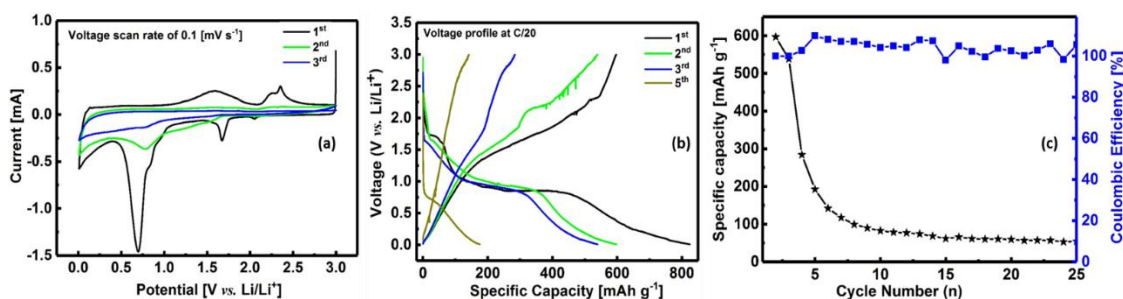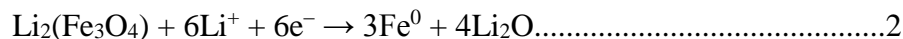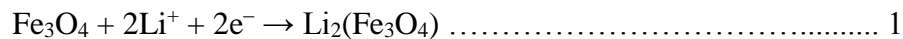

Figure 6.9: Electrochemical performance of the nanocomposite FC (a) cyclic Voltammograms curves for initial three cycles at the scan rate of 0.1 mV s^{-1}, (b) Galvanostatic lithiation/delithiation cyclic voltage profiles, and (c) variation of specific capacities and coulombic efficiency with cycle number.

Similarly, the cyclic Voltammograms for the nanocomposite M2FOC at three cycles are shown in Fig. 6.10 a. During the first discharging cycle, two reduction peaks were observed at about 0.28 and 0.72 V (*vs.* Li/Li$^+$). These peaks might be attributed to the initial lithium insertion into the Fe_3O_4 to form $Li_2Fe_3O_4$ or conversions of Fe^{2+} and

Fe^{3+} ions into Fe^0 by reduction (Fig. 6.10 a). The lithiation reaction with Fe_3O_4 occurs in

two stages:

$$Fe_3O_4 + 2Li^+ + 2e^- \rightarrow Li_2(Fe_3O_4) \dots\dots\dots\dots\dots\dots\dots\dots\dots .... 1$$

$$Li_2(Fe_3O_4) + 6Li^+ + 6e^- \rightarrow 3Fe^0 + 4Li_2O ....2$$

The cathodic peak found to be at 0.8 and 0.4 V for the second cycle, and it was

at 0.79 and 0.35 V for the third cycle. However, there was a considerable reduction in

the current intensity for the 2nd and 3rd cycles w.r.t. the 1st cycle. But, this intensity was

nearly the same for the 2nd and 3rd cycles. The shift in the voltage and decreased current

intensity may be accomplished to the volume expansion in the Fe_3O_4 present in this

composite. Such behavior was not noticed for the FC sample, which had only Fe_3C and

C phases. Further, there was a slight deviation in voltage for the 3rd cycle (in comparison

to the 2nd cycle) towards the left, which might be due to the presence of the oxide phase.

The two broad peaks were also witnessed at 1.26 and 1.6 V during the delithiation

process for the first cycle, which implied the oxidation of Fe^0 into Fe^{2+} and Fe^{3+}

respectively (Fig. 6.10 a). Nevertheless, these peaks disappeared in the subsequent

charging profiles and their discharging profiles also coincide (Fig. 6.10 a). It indicates

an occurrence of a reversible reaction and formation of a stable SEI layer over the

electrode material after the primary cycle. After the initial cycle, the CV loops for the

subsequent cycles were consistently reduced in the case of FC, whereas for the

nanocomposite M2FOC, the overlapped Voltammograms profiles implied almost

negligible structural changes after the initial cycle (Figs. 6.9 a and 6.10 a). The

Galvanostatic charging/discharging potential profiles for the sample M2FOC were

logged for the initial five cycles at a rate of C/20 and shown in Fig. 6.10 b. It displayed

a high discharge capacity of 1206 mAh g^{-1} for the first lithiation cycle and reduced to 700 mAh g^{-1} after the 5th cycle. It might have happened due to the unfavorable structural changes in the electrode material associated with the presence of Fe$_3$O$_4$. The specific discharge capacities were perceived as 1206, 824.6, 789, and 700 mAh g^{-1}, whereas the charging capacities were 860.7, 860.8, 787.4, and 706.7 mAh g^{-1} after 1st, 2nd, 3rd and 5th cycles respectively (Fig. 6.10 b, 1st and 2nd charging profiles overlapped). It is noteworthy to state that the discharge profiles did not show reversibility in the specific capacities even after five cycles. Nevertheless, with increased cycles, the charging capacity decreased. The lithiation profiles have exhibited potential plateau between 0.35-0.88 V, which might be due to the possible structural changes in the nanocomposite (Fig. 6.10 b). The width of the plateau for this sample was smaller than that for the FC sample which could be ascribed to the presence of an oxide phase (Figs. 6.9 b and 6.10 b). These findings were also supported by the CV curves which show overlapping after initial cycle for M2FOC whereas it reduced consistently for FC sample (Figs. 6.9 a and 6.10 a).
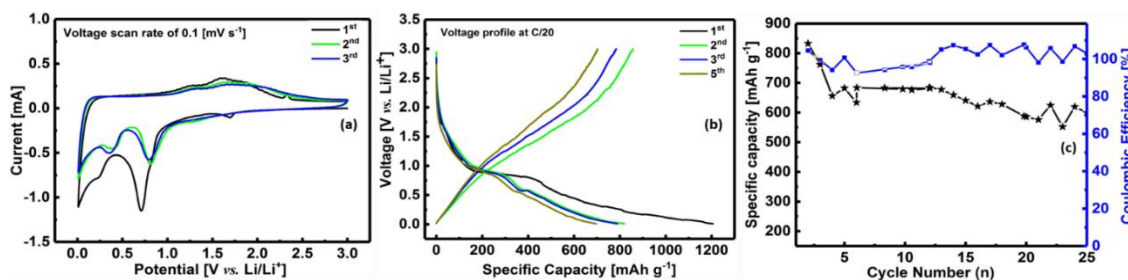

Figure 6.10: Electrochemical performance of the nanocomposite M2FOC (a) cyclic Voltammograms curves for initial three cycles at the scan rate of 0.1 mV s^{-1} (b) Galvanostatic lithiation/delithiation cyclic voltage profiles and (c) variation of specific capacities and coulombic efficiency with cycle number.

The specific charge capacity and Columbic efficiency for M2FOC *vs.* cycle numbers are described in Fig. 6.10 (c). The charge capacity found to be reducing up to 5th cycle and then remained nearly constant (~700 mAh g^{-1}) up to 11th cycles. This value then varied randomly around 600 mAh g^{-1} (Fig. 6.10 c). However, in contrast to FC, it showed better capacity, which was also suggested by the CVs profiles (Figs. 6.9 and 6.10). Moreover, the initial CE was around 71.4 % which rose to nearly 100% after a few cycles (Fig. 6.9 b and c).

Likewise, CV profiles for the nanocomposite M7FOC for the three cycles are shown in (Fig. 6.11 a). The first lithiation cycle contains two prominent cathodic peaks at 0.24 and 0.7 V (*vs.* Li/Li$^+$). These peaks were similar to that of M2FOC (Fig. 6.10 a). Nevertheless, the 2nd and 3rd lithiation cycles for this sample coincide better than the earlier sample (Figs. 6.9 a and 6.10 a). Further, the peak positions moved towards the higher potential values 0.81 and 0.4 V. The current after the 1st cycle was reduced which is also observed for other anode materials. On the other hand, during charging, a broad peak near 1.61 V was observed which implies the involved oxidation phenomenon. But, this peak disappeared after the initial cycle similar to that for M2FOC sample, which accomplishes the irreversible process (Figs. 6.10 b and 6.11 b). Even, the CV profiles merged for the 2nd and 3rd cycles specifying the reversible reaction and formation of a stable SEI layer (Fig. 6.11 b). Such layers protect the electrode against the electrolyte and retain the cyclic performance. The CV profiles (peak position and loop area) for FC, M2FOC and M7FOC continuously modified which could be attributed to the increased fraction of oxide phase (Figs. 6.1, 6.9 a, 6.10 a, and 6.11 a). Nevertheless, the effect of Mn in the system cannot be ruled out but it is hard to predict. The charge/discharge

voltage plots for M7FOC with a rate of C/20 are presented in Fig. 6.11 b. The lithium storage discharge capacity for the initial cycle was estimated as ~1261 mAh g^{-1} and diminished to ~841 mAh g^{-1} for 2nd and 3rd cycles (Fig. 6.11 b). It designates a reversible discharge capacity obtained after the primary cycle.

In contrast, the delithiated capacities for three cycles were ~ 830, 818, and 836 mAh g^{-1} for the 1st, 2nd and 3rd cycle (Fig. 6.11 b). These values were closer and hence, suggested the formation of a stable SEI as well as structural integrity during the oxidation process. The observed reversible lithiation capacity for the 2nd and 3rd cycle was also validated from their CVs curves (Fig. 6.11 a). Nevertheless, like earlier samples, this one also had a potential plateau between ~0.5-0.88 V in the discharge profile. These plateaus represent the modifications in the structure of the anode and depletion of SEI film. Amongst the samples, the width of the plateau continuously reduced with increased Mn substitutions (i.e. with increased oxide component) (Figs. 6.9 b, 6.10 b and 6.11 b). Thus, it can be inferred that the presence of oxide reduced the possible structural changes in the electrode material and gives the reversible discharge capacities for their subsequent cycles.
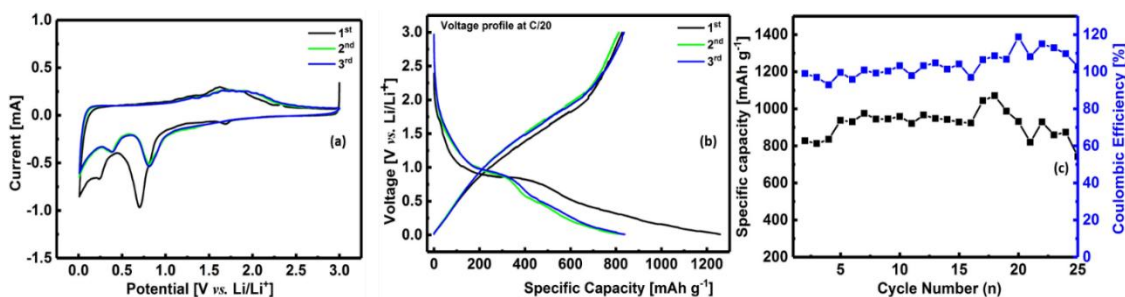

Figure 6.11: Electrochemical performance of the nanocomposite M7FOC (a) cyclic voltammograms curves for initial three cycles at the scan rate of 0.1 mV s^{-1} (b) Galvanostatic lithiation/delithiation cyclic voltage profiles and (c) variation of specific capacities and coulombic efficiency with cycle number.

For the initial cycle, the CE for M7FOC was ~65.8%, which enhanced to 97.3 and 100% respectively for 2nd and 3rd cycles (Fig. 6.11 b). It was also indicated as an overlapping of CV profiles for this sample (Fig. 6.11 a). The values of specific capacities and columbic efficiencies at various cycles for M7FOC is shown in Fig. 6.11 (c). The charge capacities and CE values were fluctuating around 826 mAh g^{-1} and 100% respectively. The literature suggest that the theoretical charge/discharge capacities for Fe_3C and graphite are 26 and 372 mAhg^{-1} respectively. However, their composite or core/shell structure have shown respective capacities of 320 mAhg^{-1} and 1226 mAhg^{-1} for 1st cycle. In contrast, the present FC sample has shown capacity of 827 and 60 mAhg^{-1} after 1st and 25th cycle respectively. Nevertheless, after 25th cycle, for M2FOC and M7FOC, the capacities had values of around 600 and 826 mAhg^{-1} respectively. This help to conclude that with increased content of oxide, the capacities also improved. As stated earlier, the oxide concentration in the composite was optimum for higher Mn substitution. The Fe_3O_4/C materials have certain drawbacks (discussed earlier) which can be overcome using Fe_3C phase. Hence, the present nanocomposite having oxide, carbide and carbon phases shown better electrochemical performance and reversibility for LIB applications.

6.3 Conclusions

In summary, the nanocomposites of Fe_3C or Mn-substituted (Fe_3C/Fe_3O_4) with carbon were synthesized successfully using a sol-gel technique followed by calcination at 700 ℃ in N_2 atmosphere. The structural and phase quantification for the composites confirmed the coexistence of three phases. The spherical morphology for the particles (5-25 nm) was confirmed by TEM analysis. The nanocomposite M2FOC displayed cell

viability more than 80 % at the concentration of 0.5 mg/mL. Further, the electrochemical performance of the nanocomposites suggested a superior reversible specific discharge capacity (~826 mAh g^{-1}) for M7FOC sample. This sample also exhibited the highest retentivity at a rate of C/20, which was established by CVs and Galvanostatic discharge/charge profiles. The improvement in the reversible specific capacities caused due to increment of the Mn content in the nanocomposite which subsequently enhanced the oxide phase. Thus, these findings suggested that the nanocomposite M7FOC can be explored as anode material for the next generation LIB$_S$ with superior energy storage capacity and high power density.